actuators

MDPI

Article

High-Rate, High-Precision Wing Twist Actuation for Drone, Missile, and Munition Flight Control

Ronald Barrett-Gonzalez * and Nathan Wolf

Aerospace Engineering Department, University of Kansas, Lawrence, KS 66045, USA
* Correspondence: adaptivebarrett@gmail.com; Tel.: +1-785-864-2226

Abstract: This paper covers a new actuation and deflection controller configuration for high-aspect-ratio wings used on subsonic drones, missiles, and munitions. Current approaches to the flight control of these aircraft have unearthed challenges with friction, stiction, slop, bandwidth, and thick boundary layer nonlinearities, which degrade flight control accuracy—especially in terminal flight phases. The approach described in this paper uses directionally attached piezoelectric (DAP) actuators to actively twist a high-aspect-ratio wing for flight control. The DAP actuators were modeled analytically and computationally using linear finite element modeling. A 3″ (7.62 cm) chord × 15″ (38.1 cm) semispan rectangular wing with an NACA 0012 profile was built and structurally tested, demonstrating excellent agreement between theory and experiment. New actuation methods were used to overdrive the PZT-5H piezoelectric elements deep into the repoling range. This overdrive actuation rejuvenated the actuator elements and allowed for dramatically improved deflections with respect to configurations in previous years. Static testing demonstrated deflections in excess of ±1.6° in root-to-tip twist. Dynamic testing showed corner frequencies greater than 310 Hz. A series of wind tunnel tests at up to 180 ft/s (55 m/s, 123 mph, 107 kts, 198 kph) demonstrated excellent roll control authority, rapid manipulation of $C_{l\delta}$, and lift manipulation using quasi-static deflections. The paper concludes with a summary of implications for terminal guidance for drone, missile, and munition flight control in real atmospheres.

Keywords: high rate; flight control; roll control; piezoelectric; missile; munition; UAV; drone

Citation: Barrett-Gonzalez, R.; Wolf, N. High-Rate, High-Precision Wing Twist Actuation for Drone, Missile, and Munition Flight Control. *Actuators* **2022**, *11*, 239. https://doi.org/10.3390/act11080239

Academic Editor: André Preumont

Received: 10 August 2022
Accepted: 16 August 2022
Published: 21 August 2022

1. Introduction

In the mid-1980s, technologists from MIT's Space Engineering Research Center made pioneering inventions and discoveries with respect to aircraft flight control. At the time, piezoelectric elements had been used for nearly 60 years as sensor and actuator elements in civil and naval structures, as well as for geophysical exploration, among other uses. One of the first of the public documents in the US to describe the sensing capabilities of piezoelectric elements was US Patent 2,212,845 (filed in 1918). This work included the lamination of piezoelectric elements to structural components so as to generate varying electrical currents in response to structural motions [1]. For more than half a century, piezoelectric elements had been used to generate sensor signals, stable crystal oscillators, and small displacements in high-rate actuator piles that were found at the cores of devices such as sonar sensors and accelerometers.

The MIT group under Prof. Ed Crawley was the first in the aerospace industry to significantly deviate from small-displacement/high-rate actuation schemes, applying piezoelectric elements to aerostructures with the goal of manipulating air loads. To do this, much larger displacements were required than the usual microstrain-level deflections. While the group would go on to fabricate a myriad of devices, perhaps their most important contribution to the field is the understanding that piezoelectric elements can be modeled as discrete layers in a laminated structure. In doing so, their behavior can be captured through simple laminated plate theory with only small adjustments accounting for piezoelectric

activity. The authors of [2] effectively "translated" the often confusing and pedantic models of piezoelectric elements enshrined by ceramicists and crystallographers into simple classical laminated plate theory (CLPT), which had been used in the aerospace industry for decades and was regularly taught at the undergraduate and graduate levels. This seminal work acted as a form of "Rosetta Stone" for many aerospace engineers, and enabled the confident integration of piezoelectric elements into a whole host of structures (it should be noted that [2] is still required reading in many adaptive structures courses taught around the world). After the establishment of the earliest laminated plate models, Crawley and Anderson used piezoelectric elements to manipulate bending moments in a cantilevered beam [3–5]. The first and most substantial patent generated by this group covering concepts that could substantially manipulate air loads was US Patent 5,374,011 by Lazarus and Crawley [6]. This patent draws upon the idea that by using anisotropic laminated plates as lifting surfaces, isometric piezoelectric elements can generate twist deformations which, in turn, can change air loads [7]. The most important of these twist-active plates is shown below.

The concept of the laminated plate above was to use laminated isotropic piezoelectric elements bonded on either side of a bending–twist-coupled graphite–epoxy plate, and then actively bend the plate using differential piezoelectric actuation. As a result, the inherent bending–twist coupling would then result in twist deformations. The plate would be oriented so that twist deformations would generate more bending deformations, which would, in turn, produce more twist. Lazarus and Crawley properly captured this very intentional aeromechanical instability, demonstrating that full flight control in roll could potentially be commanded up to divergence speeds. Excellent results were shown both on the bench and in the wind tunnel, with good correlation between theory and experiment. Although the plate shown in Figure 1 has no aerodynamic profile, it was enough to spark imaginations and research across the field, and to spawn a small industry of adaptive aerostructures research. Weisshaar's group in at Purdue University took this concept and extended the theory, leading to concepts for aeroelastic control [8]. Ehlers and Weisshaar demonstrated that wing sweep and the inherent bending–twist coupling derived from simple geometry and kinematics could also be used in conjunction with piezoelectric elements to induce aeroelastically enhanced flight control—again, with well-modeled divergence characteristics and speeds predicted.

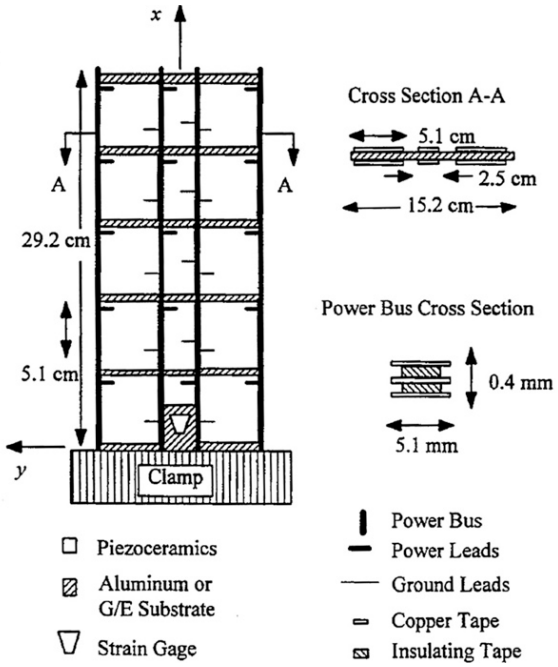

Figure 1. Schematic of the first twist-active piezoelectric aerodynamic plate [7].

The first efforts to make a piezoelectrically driven twist-active aircraft surface with an aerodynamic profile took place in 1989, with twist-active rotor blades bearing an NACA 0012 profile. Early in that year, a new sub-branch of structural mechanics had been invented. This sub-branch was centered on modifying the lamination and integration methods of active materials such as piezoelectric elements, such that isotropic materials could behave as if they were highly orthotropic. These directionally attached piezoelectric (DAP) elements would significantly change the nature of twist activation, allowing isotropic structures such as aluminum and uncoupled fiber-reinforced composite wing structures to be directly manipulated by twist. As a result, the first patent ever filed (which was also the first to generate royalties) from the US Army Rotorcraft Center of Excellence was centered on twist generation of helicopter rotor blades using DAP elements [9].

The DAP rotor blade described above was made with 7.5 mil (191 µm) thick PZT-5H piezoelectric sheets, which were cut to rhomboid shapes. Then, 128 rhomboid DAP elements were mounted on a rotor blade foam core that had been fitted with a lead leading-edge counterbalance going from 0.5 to 5% c. The PZT elements were placed from the 5% to 30% rotor blade chords so as to help keep the rotor blade's center of gravity collocated with the aerodynamic center and elastic axis, at the 25% chord. Figure 2 shows dark stripes on the piezoelectric elements, which were 2 mil (51 µm) thick Flashbreaker 1 lateral stiffness-reduction sheets. The rhomboid elements were cut and mounted at 45° on the rotor blade section, covered with style #1581 fiberglass cloth, and cured using Epolite Safe-T-Poxy at 104 °F (40 °C). The transverse stiffness-reduction sheets covered the lateral 2/3 of the piezoelectric elements, resulting in an orthotropy ratio of roughly 5.5:1. The DAP rotor blade shown above was successfully bench-, vacuum-chamber-, and whirl-stand-tested, showing comparatively small static deflections, in the order of only ±0.1° at 500 V/mm field strength (±95 V). While the static deflections were indeed small, the 27" (68.6 cm) rotor blade was aeromechanically balanced and strengthened to the point to where it was suitable for flight on a subscale rotary-wing UAV. The small deflections were clearly not suitable for primary flight control; however, with a corner frequency in excess of 250 Hz, it was clear that the blade was suitable for higher harmonic control (HHC) or other advanced structural control methods. Because the Froude-scaled blade rotational speed was 817 RPM (13.6 RPS), the blade could reach more than 18/rev actuation speed, which is more than fast enough to control all envisioned high-frequency vibration modes from the flap through to the seventh mode.

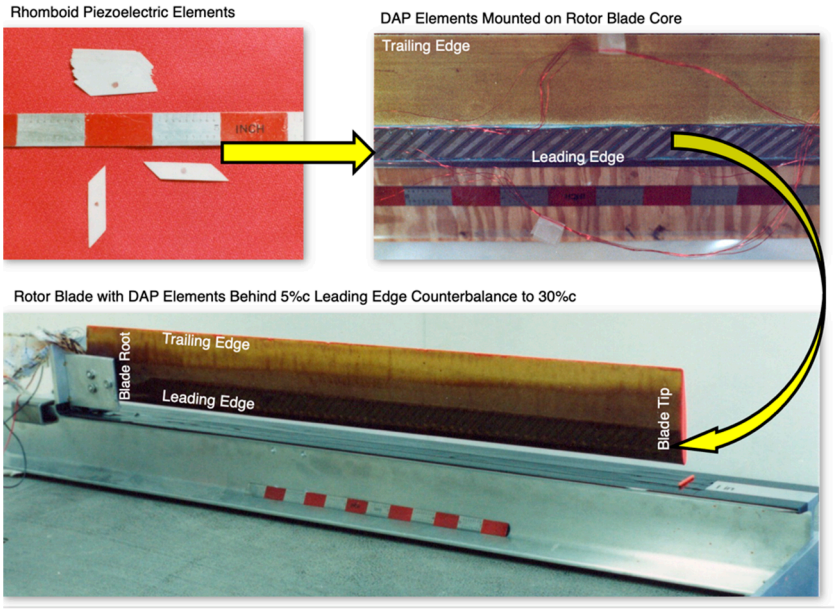

Figure 2. DAP elements and DAP rotor blade during fabrication and on the test stand [10].

While torsional blade control was being explored at the Universities of Maryland and Kansas, flap-based rotor blade control was de rigueur [11–14]. A handful of investigators explored other approaches to the induction of twist deformations to aerostructures. The most successful of these approaches was clearly the use of interdigitated electrode (IDE) piezoelectric fibers. Hagood and Bent would go on to show that individual piezoelectric fibers could be actuated to high field strengths in the poling direction (using d_{11} rather than d_{31} as is the case with DAP elements) [15,16]. This proved to be an outstanding approach to twist activation to generate high strain levels. Unfortunately, high manufacturing costs and low total fiber volume densities adversely affected its acceptance by the adaptive structures and commercial products communities.

Since those early days in the development of adaptive aerostructures, the technical community has gone on to see the development of a nontrivial number of adaptive aerostructures for many types of aircraft and spacecraft, Including adaptive latch mechanisms; flight control for missiles, munitions, and UAVs; and active noise-suppressing chevrons and stall suppression mechanisms, to name but a few [17–19].

Highly efficient PBP techniques were first seen in [20,21], as Lesieutre et al. had figured out how to drive the coupling coefficients (and, therefore, efficiencies per stroke) of piezoelectric devices close to 100% efficiency. When combining the pre-compression techniques of PBP elements with in-plane pre-compression techniques during the lamination process that had previously been developed for guided ammunition flight control actuators, a third, new method of driving emerged: limit dynamic driving (LDD). Such drivers were first used a decade ago (although they were unnamed back then) to achieve extremely high speeds, high precision, and high deflection actuation [22,23]. Since that time, LDD has been successfully used on a host of actuator classes and types. The most recent applications have been on subscale Flexspar-class piezoelectric actuators as shown below in Figure 3 [24].

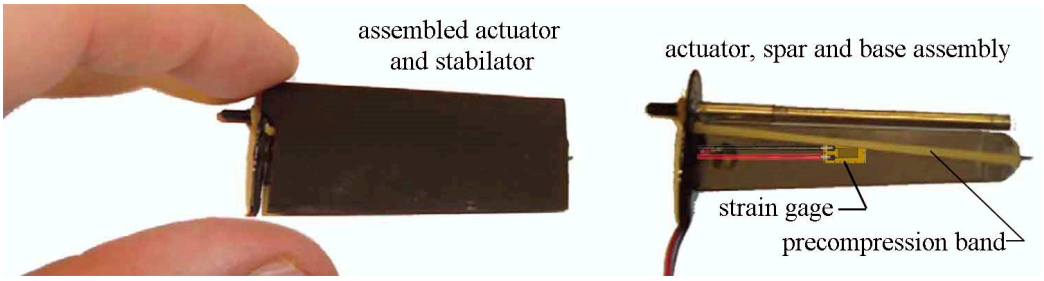

Figure 3. High-speed Flexspar actuator assembly in a micro flight control stabilator [24].

Given that modern improvements in piezoelectric actuation have evolved so dramatically, this paper is centered on applying them to twist-active aerosurface concepts to examine the performance improvements that can now be achieved.

2. Directionally Attached Piezoelectric (DAP) Modeling

One of the most successful analytical modeling techniques used to capture the behavior of DAP elements is the principle of smeared properties. This is at the heart of most laminated plate models, and has been successfully used for several decades. Once the smeared properties at the ply level are determined, they are integrated into higher-order structural constructs to develop full laminates, and then aerosurface stress–strain relations and deflections.

2.1. Fundamental DAP Effective Stiffness Modeling

The first DAP CLPT models were conceived in 1989, just after the invention of directional attachment methods [10]. In the most basic sense, the designs and modeling techniques conceived 33 years ago are still valid today, and lead to excellent smeared-properties models for the prediction of structures built with DAP elements used as actuators. An active element (in this case, a piezoelectric element) with an aspect ratio (i.e., mean length

divided by mean width) greater than 1 is attached to a substrate in such a way that the sides are free to expand and contract while the element is held firm with respect to the substrate in the lengthwise direction. In doing so, the element develops a far higher effective stiffness in the longitudinal direction than in the lateral direction. Figure 4 shows the basic geometry of DAP element integration.

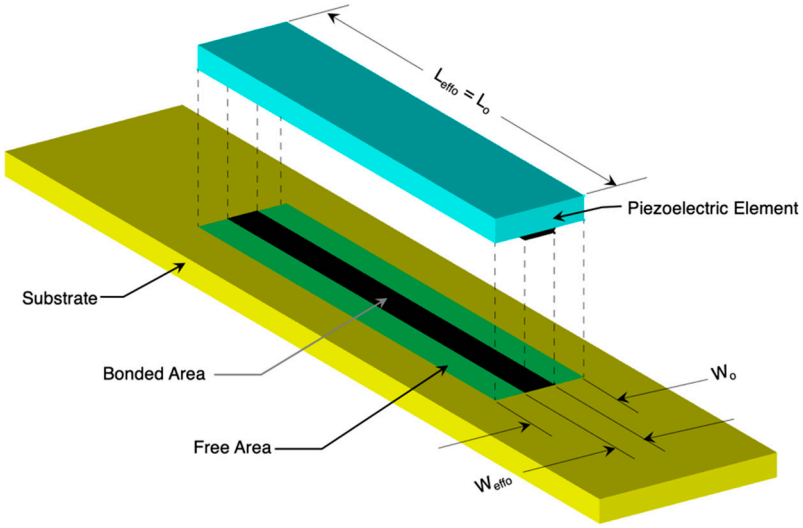

Figure 4. Basic definitions of lateral attachment geometries for DAP elements.

The modeling described in [10] determined that a reasonable approximation for the longitudinal and lateral stiffness can be achieved through directional attachment by estimating the effects of shear lag on the piezoelectric element. Once the effective longitudinal stiffness E_{Leff} and transverse stiffness E_{Teff} are determined, they can be introduced to CLPT and FEM models as actuator elements with smeared properties, as follows:

$$E_{Leff} = E_{Leffo} \frac{Sinh^{-1}\left(\frac{Sinh}{2}\left[\frac{L_{effo}}{2}\sqrt{\frac{G_{bond}}{t_{piezo}t_{bond}E_{piezo}}}\right]\right)}{\frac{L_{effo}}{2}\sqrt{\frac{G_{bond}}{t_{piezo}t_{bond}E_{piezo}}}} \quad (1)$$

The transverse ply modulus is similarly a function of geometry and bond shear moduli. As the width of the elements W_{effo} is reduced relative to the thickness of the bond, the total amount of work done by the element laterally decreases. It should be noted that the original width counted, W_{effo}, relates to the mean bond width—not the element width. By considering such geometries, the aspect ratios of both the piezoelectric element and the boding stripe come into play.

$$E_{Teff} = E_{Teffo} \frac{Sinh^{-1}\left(\frac{Sinh}{2}\left[\frac{W_{effo}}{2}\sqrt{\frac{G_{bond}}{t_{piezo}t_{bond}E_{piezo}}}\right]\right)}{\frac{W_{effo}}{2}\sqrt{\frac{G_{bond}}{t_{piezo}t_{bond}E_{piezo}}}} \quad (2)$$

The overarching goal of directional attachment is to maintain as much ply longitudinal stiffness as possible while reducing the transverse stiffness as much as possible. The result leads to a high orthotropy ratio (OR = E_{Leff}/E_{Teff}). With a reasonable amount of effort, orthotropy ratios in excess of 50 can be readily attained. OR values as low as 2 or 3 have been shown to generate good directional stress and shear strain fields, and can manipulate structures in torsion.

The effective smeared property shear modulus is accounted for similarly, with no change in the Poisson's ratios (ν_{LT}, ν_{TL}). Because the elements work longitudinally but

very little laterally, the shear moduli trend mostly with directional attachment properties in the ply longitudinal direction, as follows:

$$G_{LTeff} = G_{LTeffo} \frac{Sinh^{-1}\left(\frac{Sinh}{2}\left[\frac{L_{effo}}{2}\sqrt{\frac{G_{bond}}{t_{piezo}t_{bond}E_{piezo}}}\right]\right)}{\frac{L_{effo}}{2}\sqrt{\frac{G_{bond}}{t_{piezo}t_{bond}E_{piezo}}}} \tag{3}$$

When one accounts for end-bonding, the longitudinal stiffness ratio approaches 100%. The lateral effective stiffness is unchanged by end-bonding. It should be noted that end-bonding methods are often used not only to increase orthotropy ratios, but also to accommodate electrical leads. Given extremely high field strengths, this is important to prevent electrical breakdown on the ends. When considering DAP actuators, they can be made such that they behave as layers of active composites with nearly 100% fiber volume fractions in the longitudinal direction and 10–15% volume fractions laterally. This is substantially different from IDE layers, which tend to have fiber volume fractions of only 20–30% longitudinally, but (quite favorably) contract laterally when energized.

The local artifacts and complicated, nonlinear stress fields associated with directional attachment are smeared into properties that can then be included in highly useful global models. The first step is to integrate those properties into laminate models. Then, once in laminate models, the active laminas are then used as components in finite element models. To take the first step, the nanostructure models of directional attachment are translated into effective longitudinal, transverse, and shear moduli (E_{Leff}, E_{Teff}, and G_{LTeff}, respectively) using Equations (1)–(3), respectively. Those effective moduli are then included in classical laminated plate theory (CLPT) models of the entire laminate. By examining the work of Jones [25], the reduced stiffnesses can be calculated from the effective stiffnesses above, as follows:

$$Q_{11} = \frac{E_{Leff}}{1-\nu_{LT}\nu_{TL}} \quad Q_{22} = \frac{E_{Teff}}{1-\nu_{LT}\nu_{TL}} \quad Q_{12} = \frac{\nu_{LT}E_{Teff}}{1-\nu_{LT}\nu_{TL}} \quad Q_{66} = G_{LTeff} \tag{4}$$

The following expressions are then used to rotate the stiffnesses to laminate coordinates around the ply orientation angle θ:

$$\begin{aligned}
\overline{Q}_{11} &= Q_{11}Cos^4\theta + 2(Q_{12}+Q_{66})Sin^2\theta Cos^2\theta + Q_{22}Sin^4\theta \\
\overline{Q}_{22} &= Q_{11}Sin^4\theta + 2(Q_{12}+Q_{66})Sin^2\theta Cos^2\theta + Q_{22}Cos^4\theta \\
\overline{Q}_{12} &= (Q_{11}+Q_{22}-4Q_{66})Sin^2\theta Cos^2\theta + Q_{12}\left(Sin^4\theta + Cos^4\theta\right) \\
\overline{Q}_{16} &= (Q_{11}-Q_{12}-2Q_{66})Sin\theta Cos^3\theta + (Q_{12}-Q_{22}+2Q_{66})Sin^3\theta Cos\theta \\
\overline{Q}_{26} &= (Q_{11}-Q_{12}-2Q_{66})Sin^3\theta Cos\theta + (Q_{12}-Q_{22}+2Q_{66})Sin\theta Cos^3\theta \\
\overline{Q}_{66} &= (Q_{11}+Q_{22}-Q_{12}-2Q_{66})Sin^2\theta Cos^2\theta + Q_{66}\left(Sin^4\theta + Cos^4\theta\right)
\end{aligned} \tag{5}$$

The reduced stiffnesses of Equation (5) can then be used to solve the linear stress–strain relationships of the laminate, considering mid-plane strains ϵ^o and curvatures; κ as a function of the vertical coordinate through the laminate, as defined by Jones, yields:

$$\begin{bmatrix}\sigma_x\\ \sigma_y\\ \sigma_{xy}\end{bmatrix} = \begin{bmatrix}\overline{Q}_{11} & \overline{Q}_{12} & \overline{Q}_{16}\\ \overline{Q}_{12} & \overline{Q}_{22} & \overline{Q}_{26}\\ \overline{Q}_{16} & \overline{Q}_{26} & \overline{Q}_{66}\end{bmatrix}\left[\begin{bmatrix}\varepsilon_x^o\\ \varepsilon_y^o\\ \gamma_{xy}^o\end{bmatrix} + z\begin{bmatrix}\kappa_x\\ \kappa_x\\ \kappa_{xy}\end{bmatrix}\right] \tag{6}$$

Solving for the forces, N in the laminate in the x, y, and shear (xy) directions and the associated moments (M), as a function of the sum of all of the ply properties, yields:

$$\begin{bmatrix}N_x\\ N_y\\ N_{xy}\end{bmatrix} = \sum_{k=1}^{N}\begin{bmatrix}\overline{Q}_{11} & \overline{Q}_{12} & \overline{Q}_{16}\\ \overline{Q}_{12} & \overline{Q}_{22} & \overline{Q}_{26}\\ \overline{Q}_{16} & \overline{Q}_{26} & \overline{Q}_{66}\end{bmatrix}\left[\int_{z_{k-1}}^{z_k}\begin{bmatrix}\varepsilon_x^o\\ \varepsilon_y^o\\ \gamma_{xy}^o\end{bmatrix}dz + \int_{z_{k-1}}^{z_k} z\begin{bmatrix}\kappa_x\\ \kappa_x\\ \kappa_{xy}\end{bmatrix}dz\right] \tag{7}$$

$$\begin{bmatrix} M_x \\ M_y \\ M_{xy} \end{bmatrix} = \sum_{k=1}^{N} \begin{bmatrix} \overline{Q}_{11} & \overline{Q}_{12} & \overline{Q}_{16} \\ \overline{Q}_{12} & \overline{Q}_{22} & \overline{Q}_{26} \\ \overline{Q}_{16} & \overline{Q}_{26} & \overline{Q}_{66} \end{bmatrix} \left[\int_{z_{k-1}}^{z_k} z \begin{bmatrix} \varepsilon_x^o \\ \varepsilon_y^o \\ \gamma_{xy}^o \end{bmatrix} dz + \int_{z_{k-1}}^{z_k} z^2 \begin{bmatrix} \kappa_x \\ \kappa_x \\ \kappa_{xy} \end{bmatrix} dz \right] \quad (8)$$

From here, it is a simple matter of assembling the ABBD matrix and using such values in a finite element code such as the one described below.

2.2. Subsonic DAP Wing Geometry and Fabrication

To demonstrate the utility of DAP twist actuation for missiles, munitions, and UAVs, a 15″ (38.1 cm) semispan × 3″ (7.62 cm) chord wing was fabricated using DAP elements. In total, 120 PZT-5H elements were mounted to a foam core, as shown below. A polystyrene foam core with four flat faces was fabricated as a high-thickness substrate upon which the PZT elements and the pre-compression sheets would be mounted as shown below in Figure 5.

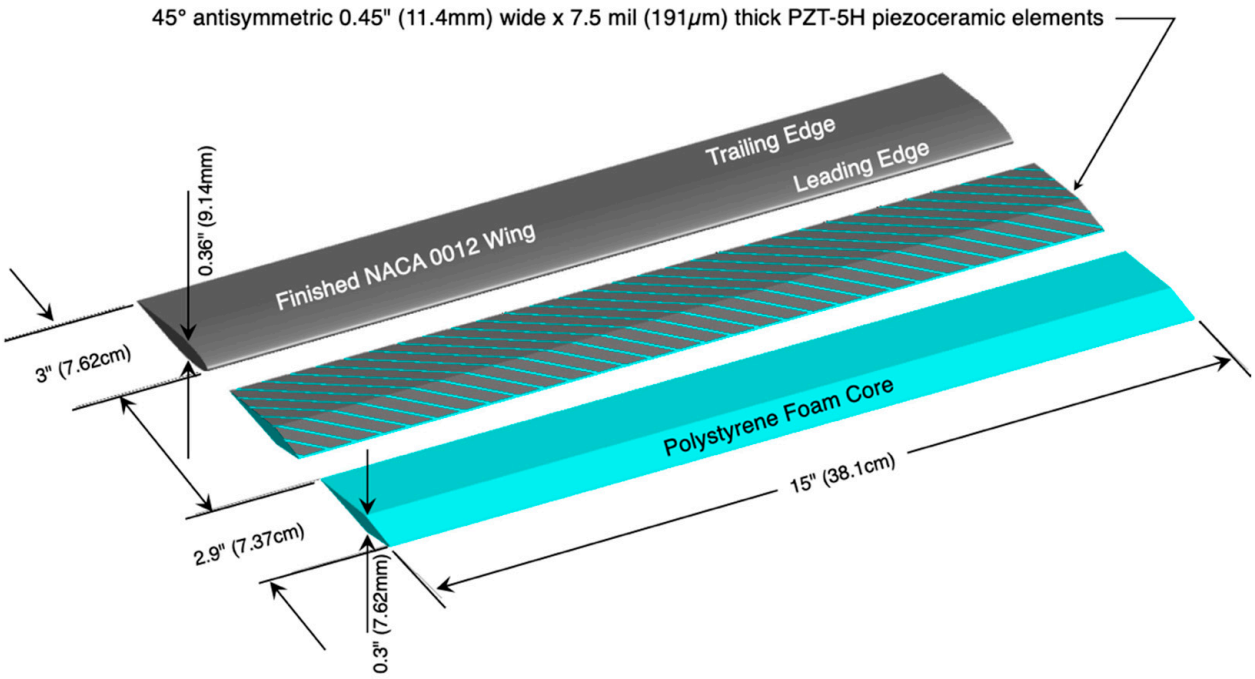

Figure 5. DAP wing build geometry and internal structural layout.

The PZT sheets were cut to 0.45″ (11.4 mm) widths (counted in the spanwise direction) and coated with 1 mil (25 μm) of Epolite Safe-T-Poxy so as to seal all of the cut edges and surfaces, except for a 0.2″ (5 mm) diameter masked area on top of the elements, which was left uncoated so as to accommodate a 1 mil (25 μm) thick dot of conducting epoxy. The PZT sheets were bonded to a 3 mil (76.2 μm) thick AISI 1100-H19 aluminum sheet with 2 mil (51 μm) thick layers of Hysol 9340 using Masterbond EP21TDC-N conducting epoxy for electrical transfer at the masked dot locations in a 180 °F (82 °C) cure under 2 bar of pressure. Following full hard curing of the laminated PZT sheets, they were bonded to the surface of the polystyrene foam core with a 1/3 directional attachment stripe oriented along the 45° element ply axis. The 120 elements were laid up antisymmetrically so as to generate simultaneous shear flows on either side of the wing surface in the same direction, with both faces working to twist the wing in the same direction, as seen below in Figure 6.

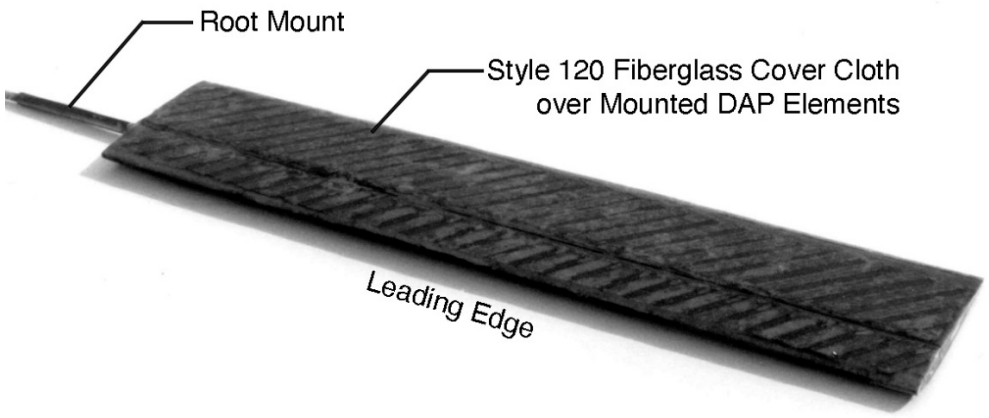

Figure 6. DAP elements under fiberglass cloth and AISI 1100-H19 pre-compression sheets bonded to a polystyrene foam core with a root connector.

The elements' poling direction was toward the foam core with the grounded side outwards, facing the wing skin. Outside of the AISI 1100 foil sheets, a style 120 fiberglass cloth oriented orthogonally was applied with Safe-T-Poxy at room temperature, and then a 50% glass bead and Safe-T-Poxy surface layer was added to bring the airfoil to surface conformity with a NACA 0012 to within 1% of the surface profile in a room temperature cure. After application and working of the glass bead layer to a profile just below the NACA 0012 profile, the wing was dipped in Safe-T-Poxy, forming a skin. The skin was then finished further to within 0.1% of the prescribed NACA 0012 profile, as seen below in Figure 7.

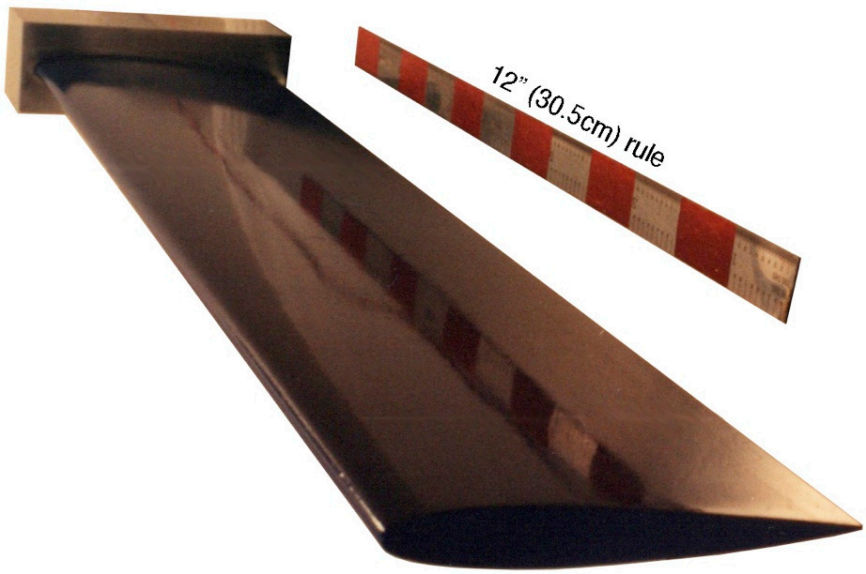

Figure 7. Finished DAP wing test specimen.

3. DAP Element Pre-Compression and Wing FEM Modeling

To execute LDD actuation techniques, the DAP elements must be highly compressed in the plane of the elements. Doing this requires a special fabrication procedure wherein coefficients of thermal expansion are used to place substrates in tension and PZT elements in compression. Following pre-compression and CLPT modeling as shown above, the smeared properties of the pre-compressed elements are then integrated into an FEM model, from which deflections are predicted

3.1. CTE Mismatch Pre-Compression Fundamentals

As described above, the PZT elements were pre-compressed in an elevated temperature-cure at 180 °F (82 °C). This placed the piezoelectric elements under roughly 550 μstrain of pre-compression at room temperature. This, of course, is necessary to provide a high level of depoling resistance to the elements, thereby further enhancing the LDD actuation. Given the stiffnesses of the actuator and the substrate (in this case, the AISI 1100-H19 foil)—E_a and E_s, respectively—a simple expression for total ply strain following pre-compression curing can be determined if one considers dramatically different coefficients of thermal expansion (α_a and α_s, respectively). The expression can easily be reduced to include a nondimensional stiffness ratio, ψ as follows:

$$\varepsilon = \frac{(E_a A_a \alpha_a + E_s A_s \alpha_s)\Delta T}{E_a A_a + E_s A_s} = \frac{(\alpha_a + \psi \alpha_s)\Delta T}{1 + \psi} \tag{9}$$

The linear coefficients of thermal expansion of the actuator and substrate (α_a and α_s, respectively) are instrumental in inducing pre-compression strain levels in the actuator elements (ε_{ap}):

$$\varepsilon_{ap} = \varepsilon - \alpha_a \Delta T = \frac{\alpha_a + \psi \alpha_s}{1 + \psi} \Delta T - \alpha_a \Delta T = \frac{\alpha_s + \alpha_a}{1 + \psi} \psi \Delta T \tag{10}$$

Similarly, the substrate pretension strain levels (ε_{sp}) can be calculated as follows:

$$\varepsilon_{sp} = \varepsilon - \alpha_s \Delta T = \frac{\alpha_a + \psi \alpha_s}{1 + \psi} \Delta T - \alpha_s \Delta T = \frac{\alpha_a + \alpha_s}{1 + \psi} \Delta T \tag{11}$$

To properly design such a wing for tactical conditions, it would be necessary to examine the minimum storage and operational temperatures to make sure that the tensile failure modes in the substrate, compressive limits of the piezoelectric element, and shear stress limits of the bond are not breached.

3.2. Integrating the Pre-Compressed DAP Elements into Finite Element Code

Considering the properties of PZT-5H and applying directional attachment methods as mentioned above, a smeared property model of the laminate skin was built within a Cosmos™ finite element model. Cosmos™ is an industry-standard FEM code that is capable of handling a wide variety of finite-element-based problems (beyond just simple linear mechanics) [26]. The moduli of the polystyrene layer and the glass sphere layer were neglected, as their stiffnesses were several orders of magnitude below those of the piezoelectric actuator and fiberglass layers. The aluminum pre-compression and piezoelectric layers had roughly matched isotropic in-plane stiffnesses. That said, together, they were modeled as smeared property DAP elements with 1/3 attachments, presenting orthotropy ratios of approximately 8.5. An exaggerated deflection model of torsional deflections at 200 μstrain free piezo strain is shown below in an 1800-element converged solution model, shown in Figure 8. The FEM model of the twist-active wing was composed of 900 elements per side divided into 20 elements per square inch (10 elements in a chordwise direction by 2 elements in a spanwise direction, in rectangular elements). The reason for the mismatch in element spacing between the span and chord was so as to capture the effects of the airfoil curvature and nose radius. Without such fine resolution, the model was shown to have broken down for elements in a coarser, chordwise direction, with converged solutions proving impossible.

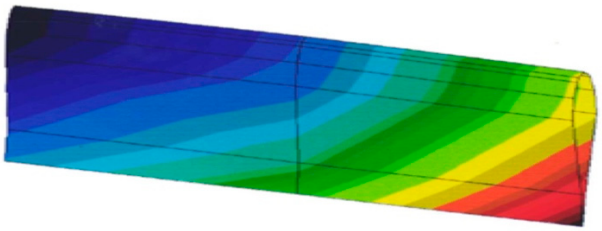

Figure 8. An 1800-element finite element torsional deflection model of a DAP wing at 200 μstrain of commanded free-strain deflections by DAP elements.

The nonlocal finite element method (NL-FEM) used in this study relies on the assumption that the postulated nonlocal elastic behavior of the material is modeled by a given element endowed with a particular set of cross-stiffness element matrices that are able to interpret the nonlocality effects induced in the particular element itself by the other elements distributed throughout the mesh. For the DAP wing using a COSMOS™ /m 2.6 FEM package (Dassault Systèmes SE, Vélizy-Villacoublay, France), an Eringen-type nonlocal elastic model is assumed with a constitutive stress–strain law of convolutional type, with smeared properties as described above, which governs the nonlocal material behavior. The excellent correlation between theory and experiment presented in Section 5 confirms the integrity of the approach.

The electromechanical coupling properties employed in [22–24] were also employed for PZT-5H operating in extreme fields under high local stresses.

4. Experimental Benchtop Testing

The wing was tested on the bench in several ways. First, weight, inertias, and electrical characteristics were measured. The wing weight (without root mount) was 10 oz (283 g). The measured quiescent capacitance was 72 μF, and the DC resistance was 1.4 MΩ, considering all DAP elements wired in parallel. The center of gravity and the elastic axis were collocated at the 36% chord with a mass moment of inertia (Iyy) of 0.31 lbm-in^2 (91 kg-mm^2) measured about the center of gravity (which was constant along the span). Torsional loads were applied to the tip to measure the passive, open-lead torsional stiffness. Loads from 1.00 in-lb (0.113 N-m) to 12 in-lbf (1.35 N-m) were applied to the wing tip. Root and tip torsional deflections were measured by laser reflection techniques, as shown below in Figure 9.

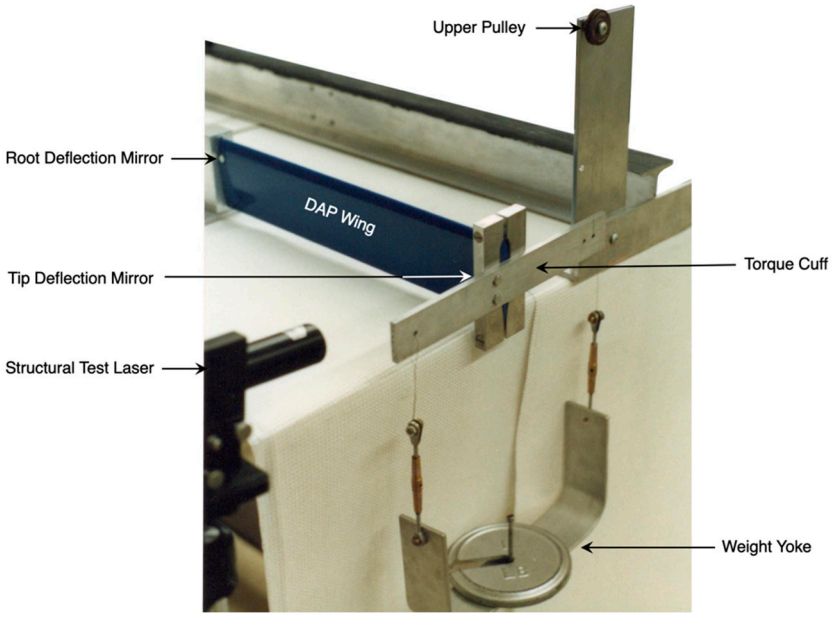

Figure 9. Wing torsional stiffness test rig.

The test results showed a linear torsional stiffness of 269 in-lbf/rad (4.69 in-lbf/deg, 30.4 N-m/rad, 0.53 N-m/deg), which was consistent with the predicted value of 4.1 in-lbf/deg. Quasi-static deflection testing was conducted at 1 Hz. LDD methods were applied to the drivers, taking advantage of the 550 μstrain pre-compression values and the high level of resistance to depoling provided by the adverse applied fields. Considering LDD applied field limits of +1800 V/mm in the poling direction across the DAP elements and −230 V/mm against the poling direction, the following results were obtained from quasi-static fields:

From Figure 10, it is clear that the use of smeared properties via DAP modeling and FEM methods can be combined, leading to reasonably accurate models—in this case, within 3.5%. Dynamic testing was conducted using a sinusoidal LDD signal and the aforementioned limits. Figure 11 shows the dynamic response of the wing to an actuation field of 450 V/mm. At 450 V/mm, the 191 μm thick PZT elements were operating at 86 V. (As an aside, aircraft systems such as those found in commercial aircraft regularly operate at many hundreds of volts (DC and AC)).

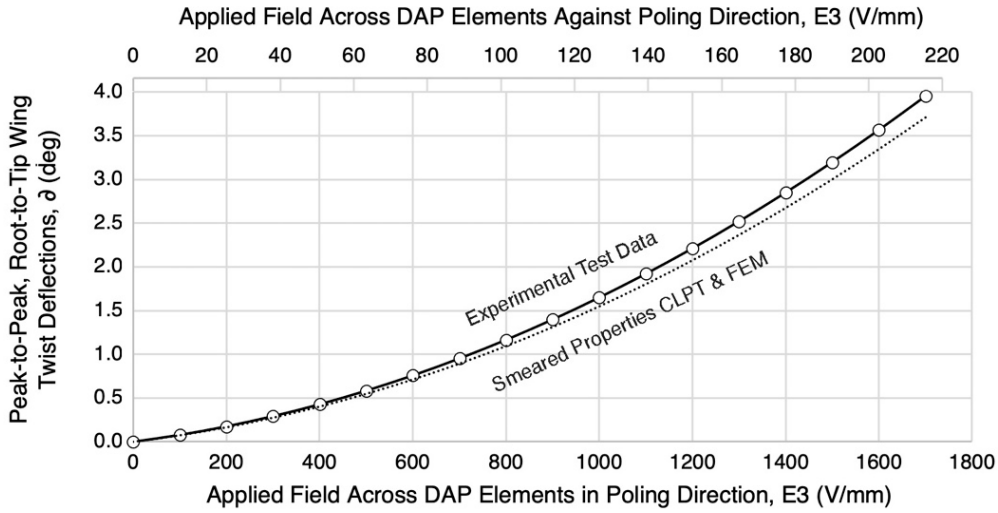

Figure 10. Quasi-static twist deflection results.

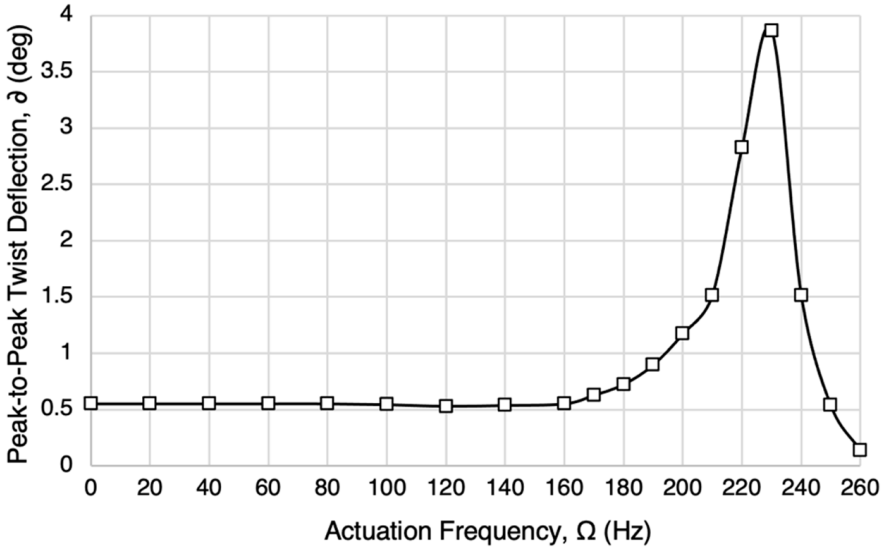

Figure 11. Dynamic twist actuation at 450 V/mm field strength.

5. Wind Tunnel Testing

The wing was mounted in the University of Kansas' 21 × 30″ (53.3 × 76.2 cm) open-circuit wind tunnel for aerodynamic testing. The wing was placed on a boundary-layer splitter plate and instrumented to measure the rolling moment coefficient about the wing root, as a twist-active wing is the most useful in roll control. Data were collected at a rate of 1 kHz with 32-bit resolution via six channels. Rolling moments about the wing root were determined via instrumented load cells, and testing was conducted from 20 ft/s up to 160 ft/s in the open-circuit wind tunnel as shown below in Figure 12. Testing at 0 ft/s airspeed concluded that the collocation of the lines of elastic axes and the centers of gravity at the 36% chord eliminated the corruption of high-frequency rolling moment measurements, which could have been induced by high rate of local pitch angle changes (due to dynamic twist) had the two not been collocated. The total measured rolling moments due to even the highest rates measured (300 Hz) were under 0.01 in-lb (0.001 N-m) (the lower limit of moment resolution for the load cells used).

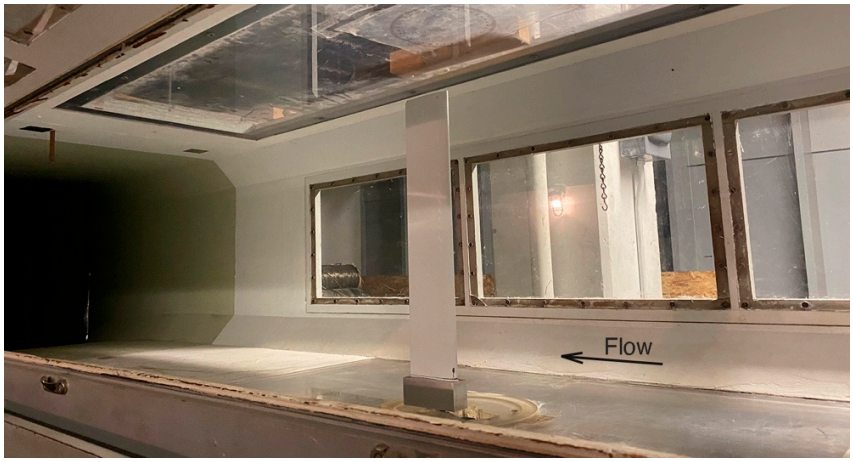

Figure 12. DAP wing mounted in the 21 × 30″ (53.3 × 76.2 cm) wind tunnel at the University of Kansas (USA) Aerospace Engineering Department.

The first series of wind tunnel tests were conducted to verify that aerodynamic pitch damping would have a negligible effect on the pitch deflections commanded during a step change in the applied field. The stiffness of the wing was so great that the differences in root-to-tip wing twist between 0 and 160 ft/s (0–49 m/s) wind tunnel speeds were effectively in the noise band—below 2% of the total values. Figure 13 shows twist deflection responses from an applied step field change of 1.1 kV/mm over the DAP elements.

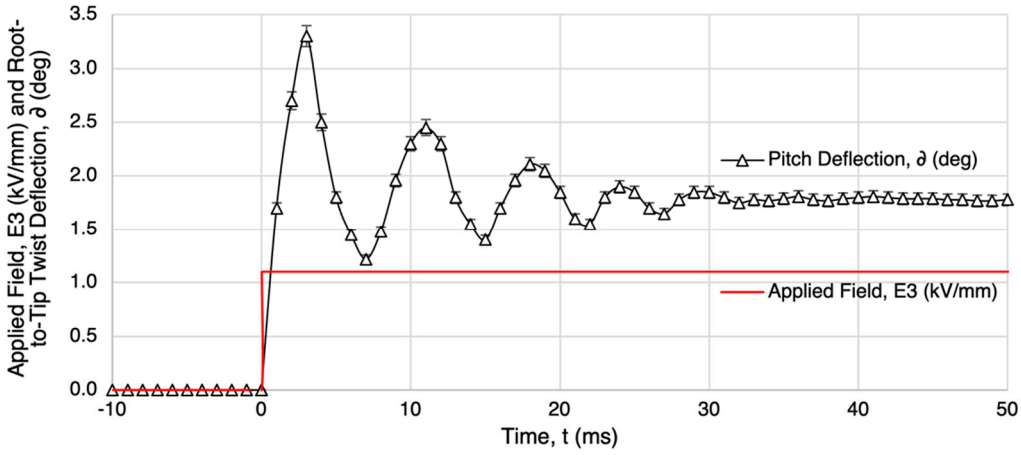

Figure 13. Root-to-tip DAP wing twist deflections with step electric field application, 0–160 ft/s (0–49m/s), Rn 0–255,000.

Figure 13 also shows comparatively little participation from other structural modes, and effectively no participation from aerodynamic loads. The collocation of the lines of elastic axes and centers of gravity effectively nullifies the primary twist–flap coupling mode. The second set of wind tunnel tests was conducted to determine the amount of roll control available as a function of flight speed (and Reynolds number). The wing was mounted in the tunnel as shown in Figure 12, and then a step field change across the piezoelectric elements was applied. The purpose of the test was to highlight a curious phenomenon that was discovered during impulse testing: dynamic lift overshoot. As the airfoil is twisted at a rapid rate, and then oscillates at a high frequency, it is postulated that a spanwise vortex is formed, which then enhances the effective camber, keeps flow attached, and produces the dynamic lift overshoot. Leishman [26–30] described just such a phenomenon occurring with rapidly pitching airfoils. Testing was conducted with the wing starting at a zero-degree angle of attack. Data were sampled at 1 kHz with moment resolutions of 0.01 in-lb (0.001 N-m) (the lower limit of moment resolution for the load cells used). Figures 14–17 show test results from 40 ft/s (12.2 m/s) to 160 ft/s (48.8 m/s), Rn = 64,000 to 255,000).

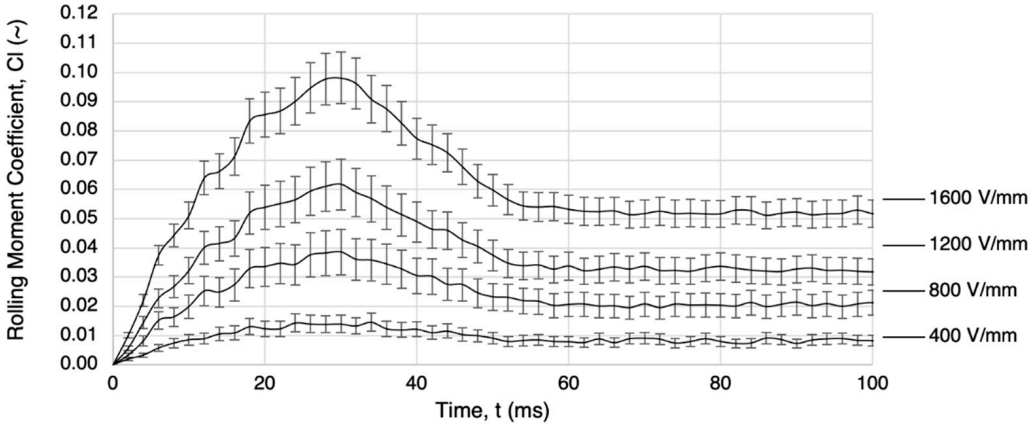

Figure 14. Rolling moment coefficient about the wing root, 40 ft/s (12.2 m/s), Rn = 64,000.

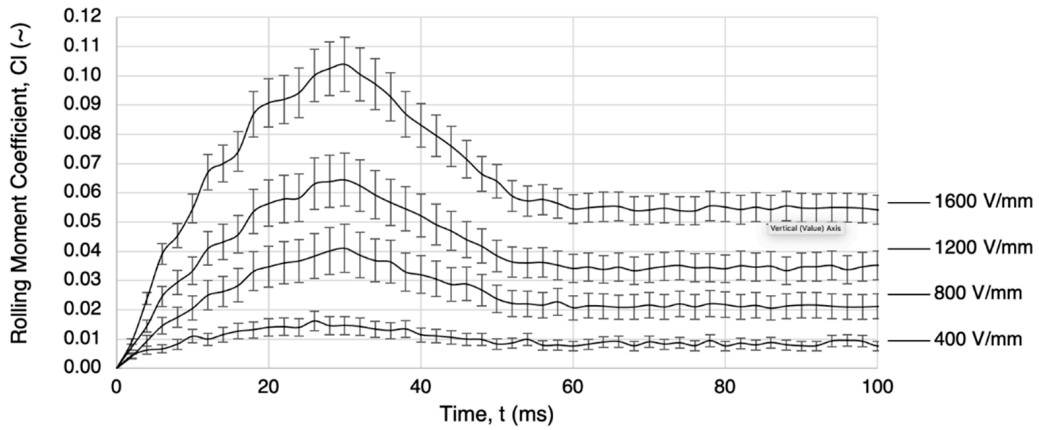

Figure 15. Rolling moment coefficient about the wing root, 80 ft/s (24.4/s), Rn = 127,000.

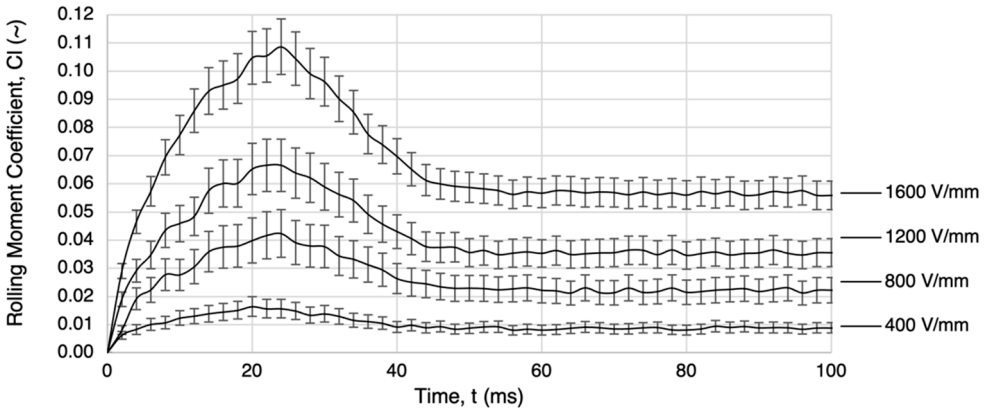

Figure 16. Rolling moment coefficient about the wing root, 120 ft/s (36.6 m/s), Rn = 191,000.

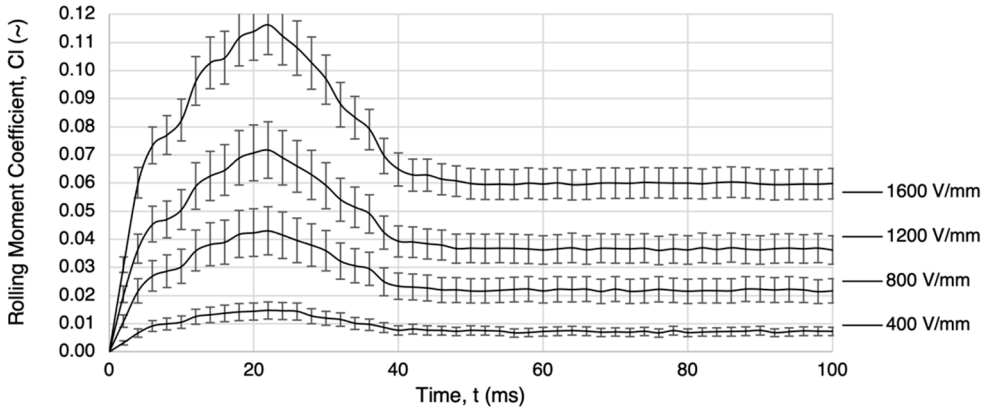

Figure 17. Rolling moment coefficient about the wing root, 160 ft/s (48.8m/s), Rn = 255,000.

One curious phenomenon observed is that the dynamic lift overshoot peak shifts to the left with increasing airspeed. This appears to be one of the first documented instances of such a pronounced dynamic lift overshoot occurring for roll control, as this phenomenon is usually seen only in helicopter rotor blades at high reduced frequencies. At 40 ft/s, the peak was observed to occur at roughly 30 ms, while at 160 ft/s, the peak shifted to 22 ms—a substantial reduction. It is thought that this is very much a function of the effects of the strength of the spanwise vorticity generated due to rapid pitch motions and exceedingly high reduced local-section pitch frequencies near the wing tip.

From Figures 14–17, it can be seen that the dynamic lift overshoot phenomenon mostly settles out by 40 ms, reaching a relatively steady state. Error bars show the range of data observed (not including standard deviation). Because of the extremely high natural frequency of the wing in torsion (228 Hz), we believe that several secondary structural modes of the tunnel mount itself were slightly excited (generating observable error bands). The flap deviations were measured below ±0.01″ (254 μm) at the 36% chord of the wing tip, and may still have been enough to contribute to the noise bands seen above. This plunge deviation is just 0.3% of the wing tip chord.

In spite of the data ranges observed, the overshoot phenomena are undeniable and nontrivial. If one examines the steady-state levels of the rolling moment coefficient and compares those levels to the peak rolling moment coefficient, it can be seen that the overshoot levels are nearly 2:1. Given that 1° of wing twist is roughly equivalent to 4–5° of aileron deflection, the amount of roll control available eclipses the control levels seen on many missile, munition, and UAV systems. What is most important is that the dynamic lift overshoot occurs precisely when a control system design engineer needs it, i.e., when high roll rates are required. This property contributes to the superior handling qualities and responsiveness of such aircraft.

6. Implications for Subscale Aircraft Flight Control

Most flight control actuators for subscale aircraft roll off at "reasonable" rates. It is rare to see flight control actuators with corner frequencies greater than 10 Hz or so. While perfectly acceptable for commercial toys and large UAVs and missiles, there is a drive for faster and faster actuation with lower levels of stiction, friction, and slop. The author of [24] showed the dynamic response of several families of commercially available subscale actuators as shown below in Figure 18.

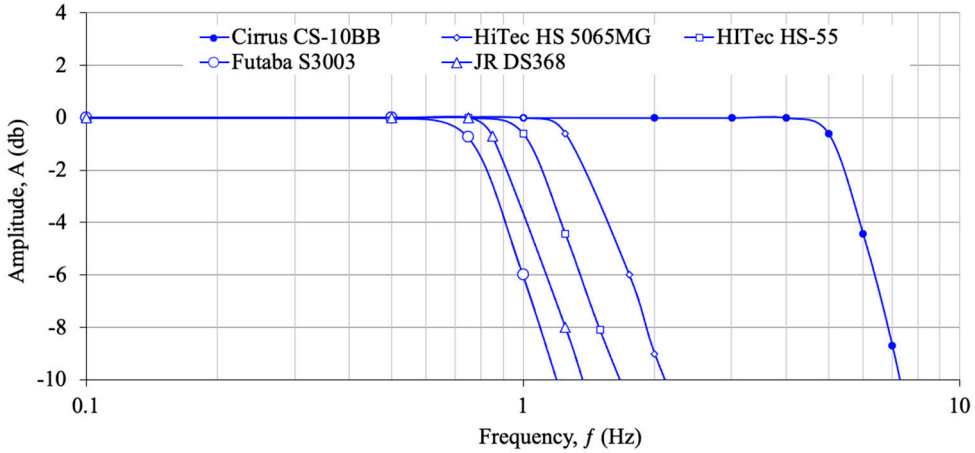

Figure 18. Typical subscale micro-servo actuator dynamic responses [24].

Because the DAP wing possesses a corner frequency in excess of 250 Hz, with levels of precision not attainable by the conventional electromagnetic actuators described above, it is ideal for precision guidance through gust fields. Such gust fields become more and more important during terminal maneuvers, and are typically only seen in hard-launched subscale munition flight control actuators [31,32].

Because mitigation of collateral damage is an extremely high priority in modern warfare, precision terminal guidance is of the utmost importance. Figure 19 shows the frequency spectrum of a typical gust field found in and around urban terrain. Given a relatively low-speed aircraft, a 0.5 kt vertical shear gust is enough to cause nontrivial terminal engagement deviation, and Figure 19 shows that such disturbances can occur as fast as 10 ms. As shown in Mil-F-8785 [33], the gust spectrum close to the ground becomes extremely robust. Low-speed aircraft will encounter high upset angles at high frequencies. Higher-speed aircraft will experience lower upset angles, but the frequency content becomes more extreme. The 255 Hz bandwidth of the DAP wing appears to be substantially faster than any fielded family of flight control actuators for missiles, munitions, and UAVs. It is so fast that not only can flight path deviations be corrected, but many buffet modes that tend to blur optics can be actively suppressed.

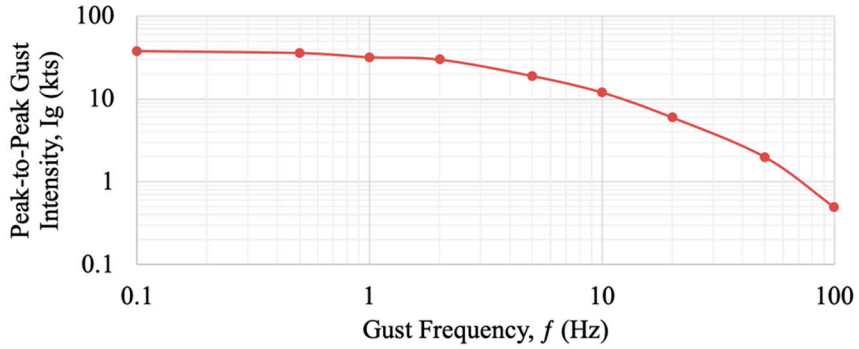

Figure 19. Urban gust field survey of power spectral density, 50% of the far-field day [24].

7. Conclusions

It can be concluded that directionally attached piezoelectric actuator elements can be successfully modeled by estimating the smear ply properties of the effects of shear lag and end-bonding on piezoelectric elements, and then integrating those smeared properties into a finite element code to estimate whole-wing torsional deflections. It was shown that a 15″ (38.1 cm) aspect ratio five-DAP airfoil could be made to achieve active twist deflections of up to 4° at rates of up to 250 Hz. It was also shown that the DAP wing could produce nearly twofold dynamic lift overshoots in rolling moment coefficients via the application of step field strength commands issued to the DAP elements. Dynamic lift overshoot peaks occurred more quickly with increasing airspeed, peaking between 22 and 30 ms after the initial command issuance. Wind tunnel testing showed root rolling moment coefficients up to $C_l = 0.06$ quiescently, with overshoot values peaking in excess of 0.115. The rate of roll control commands was shown to be nearly two orders of magnitude higher than that of the typical sub-micro servo actuators that are used in many small aircraft today, with promise to be useful for high-precision terminal guidance of munitions, missiles, gravity weapons, and stabilization of UAVs.

Author Contributions: N.W. verified the accuracy of the document and calculations. R.B.-G. performed the primary technical analysis of the contents. All of the authors contributed to the writing and proofreading of the document. All authors have read and agreed to the published version of the manuscript.

Funding: This research was funded by the University of Kansas Transportation Research Institute (KUTRI).

Institutional Review Board Statement: Not applicable.

Informed Consent Statement: Not applicable.

Data Availability Statement: Not applicable.

Conflicts of Interest: The authors declare no apparent or real conflicts of interest in the authoring of this document.

References

1. Nicholson, A. Generating and Transmitting Electric Currents. United States of America Patent 2,212,845; Filed: 10 April 1918, 27 August 1940.
2. Crawley, E.F.; Anderson, E.H. Detailed Models of Piezoceramic Actuation of Beams. *J. Intell. Mater. Syst. Struct.* **1990**, *1*, 4–25. [CrossRef]
3. Crawley, E.; Luis, J.D. Experimental Verifications of Distributed Piezoelectric Actuators for Use in Precision Space Structures. In Proceedings of the AIAA/ASME/ASCE/AHS Structurs, Structral Dynamics and Materials Conference, San Antonio, TX, USA, 19 May 1986–21 May 1986.
4. de Luis, J. *The Use of Piezo-Ceramics as Distributed Actuators in Flexible Space Structures*; Space Systems Laboratory report SSL #20-85; Aerospace Research Central: Cambridge, MA, USA, 1985.
5. Crawley, E.; Luis, J.D. Embedded Piezoelectric Structure and Control. United States of America Patent 4,849,668 Filed: 19 May 1987, 18 July 1989.
6. Lazarus, K. Multivariable Adaptive Surface Control. United States of America Patent 5,374,011, 20 December 1994.
7. Crawley, E. Induced Strain Actuation of Isotropic and Anisotropic Plates. In Proceedings of the 30th AIAA SDM Conference, Mobile, AL, USA, 3–5 April 1989.
8. Ehlers, S.; Weisshaar, T. Effect of Material Properties on Static Aeroelastic Control. In Proceedings of the 33rd AIAA Structural Dynamics and Materials Conference, Dallas, TX, USA, 13 April 1992–15 April 1992.
9. Barrett, R.M. Method and Apparatus for Structural Actuation and Sensing in a Desired Direction. United States of America Patent 5,440,193, Priority Date: 27 February 1990, 8 August 1995.
10. Barrett, R.M. Intelligent Rotor Blade and Structures Development Using Directionally Attached Piezoelectric Crystals. Master's Thesis, The University of Maryland, College Park, MD, USA, 1990.
11. Spangler, R.L.; Hall, S.R. Piezoelectric Actuators for Helicopter Rotor Control. In Proceedings of the 31st AIAA Structures, Structural Dynamics and Materials Conference, Long Beach, CA, USA, 2 April 1990–4 April 1990.
12. Spangler, R.L. Piezoelectric Actuators for Helicopter Rotor Control. Master's Thesis, Massachusetts Institute of Technology, Cambridge, MA, USA, 1989.

13. Walz, C.; Chopra, I. Design, Fabrication, and Testing of a Helicopter Rotor Model with Smart Trailing Edge Flaps. In Proceedings of the AIAA/ASME/ASCE/AHS/ASC 35th Structures, Structural Dynamics, and Materials Conference, Adaptive Structures Forum, Hilton Head, South Carolina, CA, USA, 21 April 1994–22 April 1994.
14. Been-Zeev, O.; Chopra, I. Continued Development of a Helicopter Rotor Model Employing Smart Trailing-Edge Flaps for Vibration Suppression. In Proceedings of the SPIE Smart Structures and Materials Conference, Smart Structures and Integrated Systems, San Diego, CA, USA, 8 May 1995.
15. Bent, A.; Hagood, N.W.; Rodgers, J.P. Anisotropic Actuation with Piezoelectric Fiber Composites. *J. Intell. Mater. Syst. Struct.* **1995**, *6*, 338–349. [CrossRef]
16. Bent, A.; Hagood, N.W. Piezoelectric Fiber Composites with Interdigitated Electrodes. *J. Intell. Mater. Syst. Struct.* **1997**, *8*, 903–919. [CrossRef]
17. Barrett, R.M. Adaptive aerostructures: The first decade of flight on uninhabited aerial vehicles. In Proceedings of the Smart Structures and Materials 2004: Industrial and Commercial Applications of Smart Structures Technologies, San Diego, CA, USA, 29 July 2004; Volume 5388.
18. Barrett, R.M. 20 Years of Adaptive Aerostructures in Flying Missiles, Munitions and UAVs. In Proceedings of the ASME 2014 Conference on Smart Materials, Adaptive Structures and Intelligent Systems, Newport, RI, USA, 8–10 September 2014.
19. Barrett, R.M.; Lee, G.M. Design and testing of piezoelectric flight control actuators for hard-launch munitions. In Proceedings of the Smart Structures and Materials 2004: Smart Structures and Integrated Systems, San Diego, CA, USA, 26 July 2004; Volume 5390.
20. Lesieutre, G.A.; Davis, C. Can a Coupling Coefficient of a Piezoelectric Actuator be Higher Than Those of Its Active Material? *J. Intell. Mater. Syst. Struct.* **1997**, *8*, 857–867. [CrossRef]
21. Lesieutre, G.A.; Davis, C.L. Transfer Having a Coupling Coefficient Higher than its Active Material. United States of America Patent 6,236,143, 22 May 2001.
22. Schravendijk, M.V.; Groen, M.; Vos, R.; Barrett, R.M. Closed-Loop Control for High Bandwidth, High Curvature Post-Buckled Precompressed Actuators. In Proceedings of the 50th AIAA/ASME/ASCE/AHS/ASC Structures, Structural Dynamics, and Materials Conference, Palm Springs, CA, USA, 4 May 2009–7 May 2009.
23. Groen, M.; Schravendijk, M.V.; Barrett, R.; Vos, R. Advanced control techniques for post-buckled precompressed (PBP) flight control actuators. In Proceedings of the SPIE Smart Structures and Materials + Nondestructive Evaluation and Health Monitoring, San Diego, CA, USA, 6 April 2009.
24. Barrett, R.M. High Speed Microactuators for Low Aspect Ratio High Speed Micro Aircraft Surfaces. *Actuators* **2021**, *10*, 265. [CrossRef]
25. Jones, R. *Mechanics of Composite Materials*; Hemisphere: New York, NY, USA, 1975.
26. Leishman, J.G. Contributions to the Experimental Investigation and Analysis of Aerofoil Dynamic Stall. Ph.D. Dissertation, University of Glasgow, Glasgow, UK, 1984.
27. Leishman, J.G. Validation of approximate indicial aerodynamic functions for two-dimensional subsonic flow. *AIAA J. Aircr. vol.* **1988**, *25*, 914–922. [CrossRef]
28. Leishman, J.G. *Principles of Helicopter Aerodynamics*, 2nd ed.; Cambridge University Press: New York, NY, USA, 2005.
29. Leishman, J.G. Modeling of subsonic unsteady aerodynamics for rotary wing applications. *J. Am. Helicopter Soc.* **1990**, *35*, 29–38. [CrossRef]
30. Tyler, J.C.; Leishman, J.G. Analysis of Pitch and Plunge Effects on Unsteady Airfoil Behavior. *J. Am. Helicopter Soc.* **1992**, 69–82. [CrossRef]
31. Stutts, J.; Barrett, R. Development and Experimental Validation of a Barrel-Launched Adaptive Munition. In Proceedings of the 39th Structures, Structural Dynamics and Materials Conference, Long Beach, CA, USA, 20–23 April 1998; p. AIAA-98-2037.
32. Barrett, R. Design and Testing of Piezoelectric Flight Control Actuators for Hard-Launch Munitions. In Proceedings of the Society of Photo-Optical Instrumentation Engineers 11th Annual International Symposium on Smart Structures and Materials, San Diego, CA, USA, 26 July 2004.
33. US Government Printing Office. *MIL-F-8785, Military Specification: Flying Qualities of Piloted Airplanes*; US Federal Government: Washington, DC, USA, 1968.